A large-eddy simulation analysis of collective wind farm axial-induction set points in the presence of blockage

Théo Delvaux and Johan Meyers

Departement of Mechanical Engineering, KU Leuven, Celestijnenlaan 300 - box2421, B-3001 Leuven, Belgium

Correspondence: Théo Delvaux (theo.delvaux@kuleuven.be)

Abstract. Over the past few years, numerous studies have shown the detrimental impact of flow blockage on wind farm power production. In the present work, we investigate the benefits of a simple collective axial-induction set points strategy on power maximization and load reduction in the presence of blockage. To this end, we perform a series of large-eddy simulations (LES) over a wind farm consisting of 100 IEA 15MW turbines, and build the wind farm power and thrust coefficient curves under three different conventionally neutral boundary-layer and one truly neutral boundary-layer. As a result of the large-scale effects, we show that the wind farm power and thrust coefficient curves significantly deviate from those of an isolated turbine. We carry out a trade-off analysis and determine that, while the optimal thrust set-point is still correctly predicted by the Betz limit under wake-only conditions, it shifts towards lower operating regimes under strong blockage conditions. In such cases, we observe a minor power increase with respect to the Betz thrust-set point, accompanied by a load reduction of about 5%. More interestingly, we show that for some conditions the loads can be reduced by up to 19%, at the expense of a power decrease of only 1%.

1 Introduction

Due to various constraints related to infrastructure costs, land regulations and grid connection, wind turbines are often gathered in wind farms. However, such configuration introduces non-negligible coupling between the turbines as upstream rows shed wakes on their downstream counterparts. This results in a large proportion of turbines in the farm facing lower incoming velocities and higher levels of turbulence intensity. Therefore, the design of an optimal wind farm operating strategy has been the focus of numerous research works (Steinbuch et al., 1988; Gebraad, 2014; González et al., 2015; Fleming et al., 2017; Annoni et al., 2017). To date, those strategies essentially consist in adjusting either the thrust coefficients (Axial Induction Control) or the yaw angles (Wake Redirection Control) of the turbines in the farm.

Although many studies on optimal farm operating points have shown promising results, the majority of them build upon low-fidelity engineering models, in which only the wake interactions are represented. However, recent research has highlighted the excitation of gravity waves by the farm on a much larger scale, with non-negligible impacts on the total power production of the farm (Allaerts and Meyers, 2018; Lanzilao and Meyers (2022, 2024)). This is associated with an unfavorable pressure gradient that is established at the inlet of the farm, leading to the so-called blockage effect.

To represent the wind-farm-induced pressure effects on the upstream flow, Allaerts and Meyers (2019) developed an atmospheric perturbation model. With this model, they built the farm-averaged power-coefficient curve for two sets of flow conditions. In both cases, they observed a significant drop with respect to the predictions of the wake-only models. In the work of Allaerts and Meyers (2019), only homogeneous distributions of the thrust coefficient were considered. Later, Lanzilao and Meyers (2021) proposed a more advanced optimization procedure of the wind farm thrust set point under specified flow conditions. The authors leveraged the analytical form of the model of Allaerts and Meyers (2019) to derive its adjoint gradient, with which they retrieved the optimal thrust coefficient distributions over the farm. Overall, they observed power gains larger than 4% in the majority of the tested cases. More generally, their work emphasized the important part played by gravity-wave-induced blockage effects in the design of an optimal wind farm thrust set point. However, the approach proposed by Lanzilao and Meyers (2021) relied on a box-function wind farm force, with which the interactions between the turbines could not be accurately described. Using coupled wake-blockage models, Bossanyi and Bleeg (2024) recently pointed out that axial-induction control could reduce blockage and wake effects simultaneously.

In this context, the present work aims at providing solid evidence of the benefits that can possibly be achieved through collective wind farm axial-induction control of the thrust set point. For that purpose, we build the power-coefficient and thrust coefficient curves of a large wind farm using high-fidelity LES. In this analysis, we investigate the impact of the atmospheric conditions on the shape of the curves by considering four sets of flow conditions. Due to their high computational cost, LES data of full wind farm flows are scarce. Therefore, to the best of our knowledge, no similar study has been performed before.

The remainder of this paper is organized as follows. In Sec. 2, we introduce the set of governing equations, the boundary conditions, the numerical specifications as well as the different tested cases. Sec. 3 then provides details on the precursor and spin-up phases preceding the actual simulations. The results of those last simulations are discussed in Sec. 4, in terms of the flow fields and the wind farm performances.

2 Methodology

In this section, we introduce the equations governing the LES simulations and we give a brief description of the flow solver used (Sec. 2.1). We then discuss the characteristics of the turbines and their representation in the numerical frame (Sec. 2.2). The boundary conditions selected in the scope of this study are described in Sec. 2.3 and further details about the numerical set-up are provided in Sec. 2.4. Eventually, the different atmospheric conditions and turbine thrust set points investigated in this work are summarized in Sec. 2.5. We emphasize that the methodology described below is, to a large extent, inspired by the one followed by Lanzilao and Meyers (2024).

2.1 Governing equations

Throughout the present work, the three-dimensional filtered velocity field is described by the incompressible Navier-Stokes equations. The Boussinesq approximation is used, and we employ a transport equation for the filtered potential temperature. The set of equations is explicitly given in App. A and an in-depth description of it can be found in Allaerts and Meyers (2017).

Within this paper, we focus on barotropic flows, in which a constant background pressure gradient across the domain balances the Coriolis force above the capping inversion, resulting in a geostrophic wind in the free atmosphere that is constant with height. Moreover, the forcing exerted by the turbines on the flow (see Sec. 2.2) is accounted for through an actuator disc model (ADM). With regard to the subgrid-scale model, we use the stability-dependent Smagorinsky model developed by Stevens et al. (2000). The corresponding Smagorinsky coefficient is set to $C_s = 0.14$, similar to previous works carried out with SP-Wind (Goit and Meyers, 2015; Allaerts and Meyers, 2017; Munters and Meyers, 2018 and Lanzilao and Meyers (2023, 2024)). Moreover, we use the damping approach of Mason and Thomson (1992) near the wall, which is a well established technique for neutral ABL's (see also Meyers, 2011).

In order to solve the set of equations, we use the in-house SP-Wind solver (see, e.g., Calaf et al., 2010; Goit and Meyers, 2015; Allaerts and Meyers (2017, 2018); Munters and Meyers, 2018 and Lanzilao and Meyers (2022, 2023)). This software relies on a classical fourth-order Runge-Kutta scheme with a Courant-Friedrichs-Lewy number of 0.4 to integrate the system in time. At every stage of the numerical scheme, the Poisson equation is solved to ensure continuity. Further, SP-Wind provides pseudo-spectral Fourier schemes that are used to discretize the equations along the streamwise and spanwise directions. We note that aliasing errors are prevented thanks to the $3/2$ dealiasing rule of Canuto et al. (1998). Finally, the vertical direction is discretized following an energy-preserving fourth-order finite difference scheme, as discussed in Verstappen and Veldman (2003). The reader can refer to, e.g., Delport (2010) for further details about the discretization employed.

2.2 Wind turbine characteristics

In this paper, we model the performances of the IEA 15-Megawatt offshore turbine detailed by Gaertner et al. (2020). It is equipped with a rotor of diameter $D = 240\,\mathrm{m}$ located at hub height $z_H = 150\,\mathrm{m}$ that delivers a rated power of $P_r = 15\,\mathrm{MW}$.

We model the turbine rotor as a non-rotating actuator disc, similarly to the LES studies of Allaerts and Meyers (2015), Goit and Meyers (2015), Lanzilao and Meyers (2022, 2023, 2024), among others. In the actuator disc model, the turbine acts as an infinitely thin disc that extracts momentum from the flow. However, in order to prevent numerical instabilities associated with abrupt gradients of forces, we smooth out the force distribution by means of a Gaussian filtering operation (Calaf et al., 2010; Meyers and Meneveau, 2010). We define the three dimensional Gaussian filter as

$$G(\mathbf{x}) = \left(\frac{6}{\pi\Delta_f^2}\right)^{3/2} \exp\left[-6\frac{x^2+y^2+z^2}{\Delta_f^2}\right], \tag{1}$$

where $\mathbf{x}$ denotes the coordinate vector and Δ_f is the filter width. In SP-Wind, the filter width relates to the grid spacing through $\Delta_f = \max\{f_x\Delta x,\, f_y\Delta y,\, f_z\Delta z\}$, with $f_x = f_y = f_z = 1.5$ the filter parameters, and $\Delta x, \Delta y$ and Δz the cell dimensions discussed in Sec. 2.4. Consequently, the footprint for a turbine centered at $\mathbf{x_t}$ corresponds to (Meyers and Meneveau, 2010)

$$\mathcal{R}(\mathbf{x}) = \iiint_{\Omega} G(\mathbf{x}-\mathbf{x}')\,\delta\left[(\mathbf{x}'-\mathbf{x_t})\cdot\mathbf{e}_\perp\right]\mathcal{H}(D/2 - ||\mathbf{x}'-\mathbf{x_t}||_2)d\mathbf{x}', \tag{2}$$

with $\mathbf{e}_\perp$ the unit vector orthogonal to the turbine and Ω the three dimensional space. In Eq. 2, the symbols δ and $\mathcal{H}$ represent the Dirac delta distribution and the Heaviside function, respectively.

Then, the velocity at the location of the k^{th} rotor and perpendicular to it is computed as the spatial average over the footprint:

$$u_{d,k} = \frac{M}{A} \iiint\limits_{\Omega} \mathcal{R}(\mathbf{x})\, \mathbf{u} \cdot \mathbf{e}_{\perp} d\mathbf{x}, \tag{3}$$

where $A = \pi D^2/4$, and M is the velocity correction factor (Shapiro et al., 2019). For coarse grids, the filtering operation may lead to a power over-estimation as the rotor diameter appears to be artificially increased. Therefore, we use the velocity correction factor M proposed by Shapiro et al. (2019) as a function of the filter width Δ_f and the disc-based thrust coefficient C_T':

$$M = \left(1 + \frac{C_T'}{2} \frac{1}{\sqrt{3\pi}} \frac{\Delta_f}{D}\right)^{-1}. \tag{4}$$

Furthermore, the magnitude of the thrust force exerted by the k^{th} rotor,

$$F_k = \frac{1}{2} \rho_0 C_{T,k}' u_{d,k}^2 \frac{\pi}{4} D^2, \tag{5}$$

is distributed over the turbine footprint as done by Meyers and Meneveau (2010),

$$f_k(\mathbf{x}) = F_k \mathcal{R}(\mathbf{x}), \tag{6}$$

where ρ_0 is the reference air density and $u_{d,k}$ the local disc-averaged velocity (Eq. 3). Further, the force intensity is set through the disc-based thrust coefficient denoted C_T', the value of which is given as input to SP-Wind (see Sec. 2.5). Similarly to Allaerts and Meyers (2017) and Lanzilao and Meyers (2024), we employ a simple yaw controller that maintains the actuator disc perpendicular to the flow direction measured one diameter upstream. Consequently, we emphasize that the total force F_k (Eq. 5) is the magnitude of a vector that generally has components along both the spanwise and streamwise directions. Finally, the total power the k^{th} turbine extracts from the flow, denoted P_k, is computed as follows:

$$P_k = F_k u_{d,k} = \frac{1}{2} \rho_0 C_{T,k}' u_{d,k}^3 \frac{\pi}{4} D^2. \tag{7}$$

2.3 Boundary conditions

The boundary conditions of the numerical domain are specified as follows. On the bottom face, we model the development of shear stresses by means of the classic Monin–Obukhov similarity theory for neutral boundary-layer (Moeng, 1984; Allaerts, 2016), for which a surface roughness $z_0 = 1 \times 10^{-4}$ m representative of offshore conditions is selected.

Further, both the streamwise and spanwise lateral sides of the domain are assigned periodic boundary conditions. This allows to model an infinitely wide domain, provided that no farm-induced effects reaches the edge of the domain. The choice of an appropriate domain size is discussed in Sec. 2.4. Along the streamwise direction, we employ the wave-free fringe region technique developed by Lanzilao and Meyers (2023), in which a body-force is applied to ensure that the desired inflow conditions are imposed at the front of the domain. The generation of spurious gravity waves arising from this non-physical body-force is prevented thanks to a damping of the vertical-momentum above the ABL. The wave-free fringe-region technique is used together with a concurrent precursor approach, from which the fully developed turbulent flow field can be imposed (see Sec. 3.1).

At the top of the domain, a rigid-lid condition ensures zero shear stress, zero vertical velocity and a fixed potential temperature. Without particular treatment, however, this boundary condition significantly reflects gravity-waves. Therefore, we use a Rayleigh-damping layer (RDL) to curtail this wave reflection effect, similarly to Allaerts and Meyers (2017) and Lanzilao and Meyers (2023, 2024), among others. The method consists in applying a body force in the upper part of the free atmosphere, with an intensity proportional to the difference between the local velocity field and the geostrophic wind.

2.4 Numerical set-up

Prior to simulating the flow in the wind farm, we run a precursor simulation in which the turbulent flow fully develops and reaches a statistically steady behaviour. When running the wind farm simulation, the precursor is concurrently advanced in time so as to provide the inflow, as discussed in Sec. 2.3. In the scope of this work, we select a precursor domain with dimensions $L_x^p = L_y^p = 10\,\mathrm{km}$ and $L_z^p = 3\,\mathrm{km}$, as done by Allaerts and Meyers (2017, 2018) and Lanzilao and Meyers (2024). Next, we set the dimensions of the main domain on the basis of the observations of Lanzilao and Meyers (2024). We note that in the latter study, the authors consider a wind farm about $4\,\mathrm{km}$ longer but $2\,\mathrm{km}$ narrower than the one investigated in the present work (see Sec. 2.5). Therefore, we use the same main domain length and height as in Lanzilao and Meyers (2024), $i.e.$ $L_x \times L_z = 50 \times 25\,\mathrm{km}^2$, but we increase the domain width by 10km so that the main domain has dimensions $L_x \times L_y \times L_z = 50 \times 40 \times 25\,\mathrm{km}^3$. While the domain height may initially appear overly large, it is required to allow for the non-reflecting radiation of gravity waves and to accommodate the Rayleigh damping layer described in Sec. 2.3. The farm is symmetrically positioned along the spanwise direction, resulting in a distance of $L_{\text{side}} = 14.3\,\mathrm{km}$ between the edges of the farm and the lateral sides of the domain. Eventually, the distance upstream of the farm is taken equal to $L_{\text{ind}} = 18\,\mathrm{km}$ to allow for a full representation of the induction zone (Lanzilao and Meyers, 2024).

Because periodicity is imposed over the four lateral sides of the precursor domain, the tiling technique of Sanchez Gomez et al. (2023) is employed to extend the ten-kilometer-long and ten-kilometer-wide precursor field to the horizontal dimensions of the main domain. The resulting field is used as the initial state in the wind farm simulations. The same tiling operation, limited to the spanwise direction however, is carried out to generate the concurrent precursor with horizontal dimensions $L_x^{cp} \times L_y^{cp} = 10 \times 40\,\mathrm{km}^2$. Additionally, we artificially extend the height of the precursor field by imposing the geostrophic flow field from $3\,\mathrm{km}$ to $25\,\mathrm{km}$ for all the considered atmospheric conditions. The characteristics of the precursor field are further discussed in Sec. 3.1.

Furthermore, the grid resolution is identical to that selected by Lanzilao and Meyers (2024), that is, $\Delta x = 31.25\,\mathrm{m}$, $\Delta y = 21.74\,\mathrm{m}$ along the streamwise and spanwise directions, respectively. This corresponds to $N_x^p = 320$ and $N_y^p = 460$ grid points along the x and y axes of the precursor domain. In the main domain, the selected resolution leads to $N_x = 1600$ and $N_y = 1840$ points. Contrary to the regular grid spacing adopted in the horizontal plane, we use a height-dependent vertical discretization to reduce the computational cost. Firstly, a relatively fine constant spacing $\Delta z = 5\,\mathrm{m}$ is retained below $1.5\,\mathrm{km}$, with which the

Table 1. Magnitude (ν^{ra}), growing rate (s^{ra}) and thickness (L_z^{ra}) of the Rayleigh-damping layer. Parameters values are set following Lanzilao and Meyers (2024).

Parameter	ν^{ra}	s^{ra}	L_z^{ra}
Value	5.15	3	10
Unit	-	-	km

velocity gradients can be accurately captured. Consequently, the turbine rotor encompasses 11 and 48 grid points along the spanwise and vertical directions, respectively. We note that those values align with that of other recent similar studies (Calaf et al., 2010; Wu and Porté-Agel, 2011; Allaerts and Meyers, 2017; Lanzilao and Meyers, 2024). Secondly, the grid is smoothly stretched over 180 points in the region between $1.5\,\text{km}$ and $15\,\text{km}$. Lastly, an additional stretch is applied over 10 grid points from 15 km to 25 km. Overall, a total of $N_z = 490$ grid points is used along the vertical direction. Note that the same vertical discretization, trimmed to $L_z^p = 3\,\text{km}$, however, is adopted for the initial precursor simulation. In the region where the vertical grid spacing is the finest, the spanwise-vertical aspect ratio is equal to $\Delta y/\Delta z \simeq 4.3$. Although no detailed study on the aspect ratio impact was performed with SP-Wind, values of the order 3-to-4 were historically retained (Allaerts and Meyers, 2017; Lanzilao and Meyers (2023, 2024)) in order to account for the differences between the discretization schemes used in the spanwise and vertical directions (see Sec. 2.1).

In Sec. 4.2, the power production of an isolated turbine is compared to that of the wind farm for reference. Therefore, it is necessary to perform simulations of an identical turbine operating in stand-alone conditions. The horizontal dimensions of the corresponding main domain are the same as that of the precursor simulation, so that only the vertical extension from 3 km to 25 km is required.

Finally, as the wind farm setup and the domain size considered here are very similar to that of Lanzilao and Meyers (2024), the same settings are selected for the Rayleigh-damping-layer and for the fringe region. The corresponding values are summarized in Table 1 and Table 2, respectively. In Table 1, the first two parameters denote the magnitude and the growing rate of the RDL, whereas L_z^{ra} is the thickness of the layer. The first four parameters in Table 2 refer to the starting and ending points of the fringe region, and the corresponding smoothness coefficients, respectively. The following four parameters denote the same quantities, however related to the vertical-momentum damped region. Eventually, $h_{\max}$ characterizes the strength of the fringe function. The mathematical expressions of the Rayleigh-damping function, the fringe region forcing and the momentum damping function are given in App. B

2.5 Wind farm operating conditions

The wind farm examined in the current work consists of 100 IEA 15 MW turbines arranged in a 10-by-10 configuration. The spacing between each turbine is set to $S_x = S_y = 5\,D$ in both the spanwise and streamwise directions. We introduce an offset of $S_y/2$ between every downstream row to obtain a staggered layout. Given the turbine diameter specified in Sec. 2.2, the resulting power density is $P_r/(S_x S_y) \simeq 10.42\,\text{MW}\,\text{km}^{-2}$. Overall, the wind farm, starting at $L_{\text{ind}} = 18\,\text{km}$ (Sec. 2.4), is $L_x^f = 10.8\,\text{km}$

Table 2. Starting (x_s^h) and ending (x_e^h) points of the fringe region and corresponding smoothness coefficients (δ_s^h, δ_e^h). Starting (x_s^d) and ending (x_e^d) points of the momentum-damped region and corresponding smoothness coefficients (δ_s^d, δ_e^d). Fringe-region strength (h_{max}). Parameters values are selected following Lanzilao and Meyers (2024).

x_s^h	x_e^h	δ_s^h	δ_e^h	x_s^d	x_e^d	δ_s^d	δ_e^d	h_{max}
44.5	47.2	0.4	0.4	44.5	50	2.5	3	0.3
km	km	km	km	km	km	km	km	s^{-1}

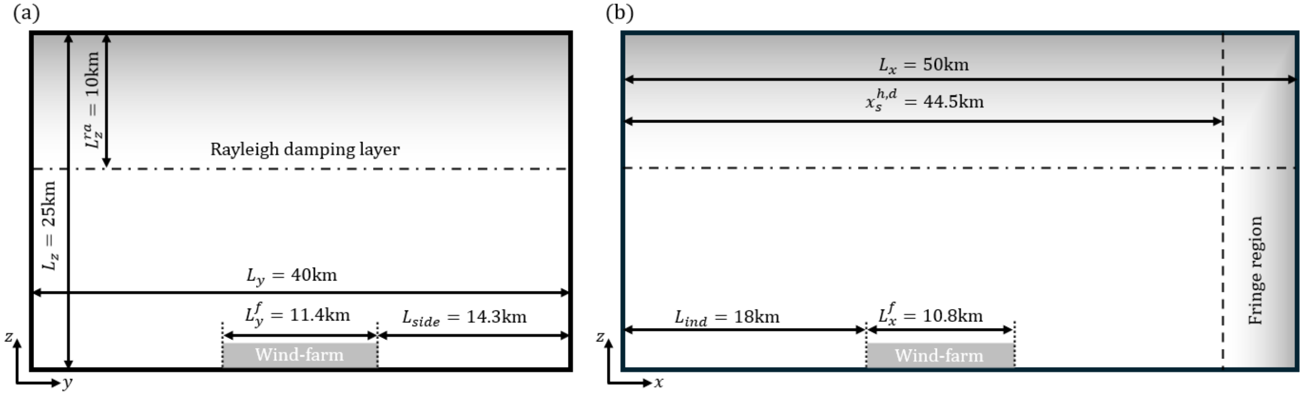

Figure 1. Scaled representation of the front (a) and side (b) views of the domain set-up employed in the wind farm simulations. The Rayleigh damping layer and the fringe region introduced in Sec. 2.4 are shown on the figure.

long and $L_y^f = 11.4\,$km wide, leading to the following ratios: $L_{\text{ind}}/L_x^f = 1.67$, $L_x/L_x^f = 4.63$ and $L_y/L_y^f = 3.51$. A sketch of the numerical domain is depicted in Fig. 1.

In order to explore the potential for power optimization and load reduction using axial induction control, different disc-based thrust coefficients (Eq. 5) are tested. From axial momentum theory, the value $C_T = 8/9$, or equivalently $C_T' = 2$ (Allaerts, 2016), maximizes power extraction. In practice, the designed thrust set point is slightly lower to reduce the associated loads at rated wind speed (Gaertner et al. 2020). In the scope of this work, we therefore select the theoretical optimal disc-based thrust coefficient, along with three other values of C_T' evenly spaced at intervals of 0.75: $C_T' = \{0.50;\ 1.25;\ 2.0; 2.75\}$. Following classical momentum theory (Allaerts, 2016), the corresponding values of the thrust coefficient are $C_T = \{0.40; 0.73; 0.89; 0.97\}$. We emphasize that in all the simulations, the considered C_T' value is constant throughout the wind plant, representing the choice of a collective thrust set point. This allows to restrict the number of parameters in the study.

To initialize the precursor simulation, a potential temperature profile is defined following the model of Rampanelli and Zardi (2004) for conventionally neutral boundary-layers (CNBL). We denote the height of the capping inversion by H and set the constant potential-temperature below it to $\theta_0 = 288.15\,$K. Further, we refer to the strength and thickness of the capping inversion as $\Delta\theta$ and ΔH, respectively. Above the capping inversion, the potential-temperature profile is controlled by the rate Γ in the free atmosphere.

Based on the observations of Lanzilao and Meyers (2024), we select a first set of parameters, $\{\mathrm{H}= 150\,\mathrm{m}$, $\Delta\theta = 8\,\mathrm{K}$, $\Gamma = 1\,\mathrm{K}$ $\mathrm{km}^{-1}\}$ (referred to as H150-$\Delta\theta8$-$\Gamma1$), for which strong blockage effects are expected to have a substantial influence on the wind farm efficiency. Lanzilao and Meyers (2024) reported a non-local efficiency lower than 0.3, however partially counterbalanced by a strong favorable pressure gradient within the farm, with which the wake efficiency becomes larger than one. In spite of this, the H150-$\Delta\theta8$-$\Gamma1$ case was observed to result in a low farm efficiency of about 32%. Secondly, we consider the scenario H300-$\Delta\theta5$-$\Gamma1$, in which blockage effect is attenuated due to a weaker capping inversion positioned at a higher altitude. Finally, we investigate the combination H500-$\Delta\theta5$-$\Gamma4$, for which Lanzilao and Meyers (2024) observed a beneficial impact of the thermal stratification on the farm efficiency. Note that for all three sets of atmospheric conditions, the capping inversion thickness is initialized to $\Delta\mathrm{H} = 100\,\mathrm{m}$. In addition to the three CNBL atmospheric conditions, we consider a situation with no thermal stratification, similar to Lanzilao and Meyers (2024). To generate this flow, we start from the case H500-$\Delta\theta5$-$\Gamma4$ and artificially set a constant potential temperature profile when copying the solution from the precursor to the main domain. The resulting flow, denoted H500-$\Delta\theta0$-$\Gamma0$, resembles a truly neutral boundary-layer (TNBL) but with the same inlet velocity as H500-$\Delta\theta5$-$\Gamma4$.

Moreover, for all the simulations performed in this analysis, we set the geostrophic wind speed to $G = 10\ \mathrm{m\,s^{-1}}$, as done by Lanzilao and Meyers (2024). We remark that this speed is slightly lower than the rated speed of the IEA 15-MW turbine reported by Gaertner et al. (2020). Consequently, this choice of geostrophic speed allows to analyze the turbine performances in the region where it typically operates at maximum thrust coefficient when following a greedy control approach. Finally, we set a latitude $\phi = 51.6\,\mathrm{deg}$, resulting in a Coriolis frequency $f_c = 1.14 \times 10^{-4}\,\mathrm{s^{-1}}$.

3 Boundary-layer initialization

The precursor phase performed to initialize the boundary-layer flow is described in Sec. 3.1. Then, the wind farm set-up introduced in Sec. 2.5 is added to the main domain and a spin-up phase is conducted until the flow reaches a quasi-steady state. The transient behavior of the flow during this second phase is discussed in Sec. 3.2.

3.1 Precursor phase

The precursor phase is carried out to obtain a statistically steady, fully developed turbulent flow over the domain. For that purpose, the initial velocity profiles are defined following the approach of Allaerts and Meyers (2015), that is, a boundary-layer flow with friction velocity $u_* = 0.26\,\mathrm{m\,s^{-1}}$ connected to a laminar geostrophic wind above the capping inversion. Turbulence is initiated by mean of divergence-free fluctuations of amplitude $G/10$ introduced up to an altitude of $100\,\mathrm{m}$. The initial potential temperature profiles are generated using the Rampanelli and Zardi (2004) model together with the sets of parameters, $\mathrm{H}, \Delta\theta$ and Γ, detailed in Sec. 2.5. We emphasize that a Rayleigh-damping layer is also applied during the precursor phase to damp the inertial fluctuations and the gravity waves above $1\,\mathrm{km}$ in the atmosphere. For each atmospheric condition, the precursor simulation is performed over 20 hours. The resulting flow quantities are then time-averaged over the last 4 hours of simulation and displayed in Fig. 2.

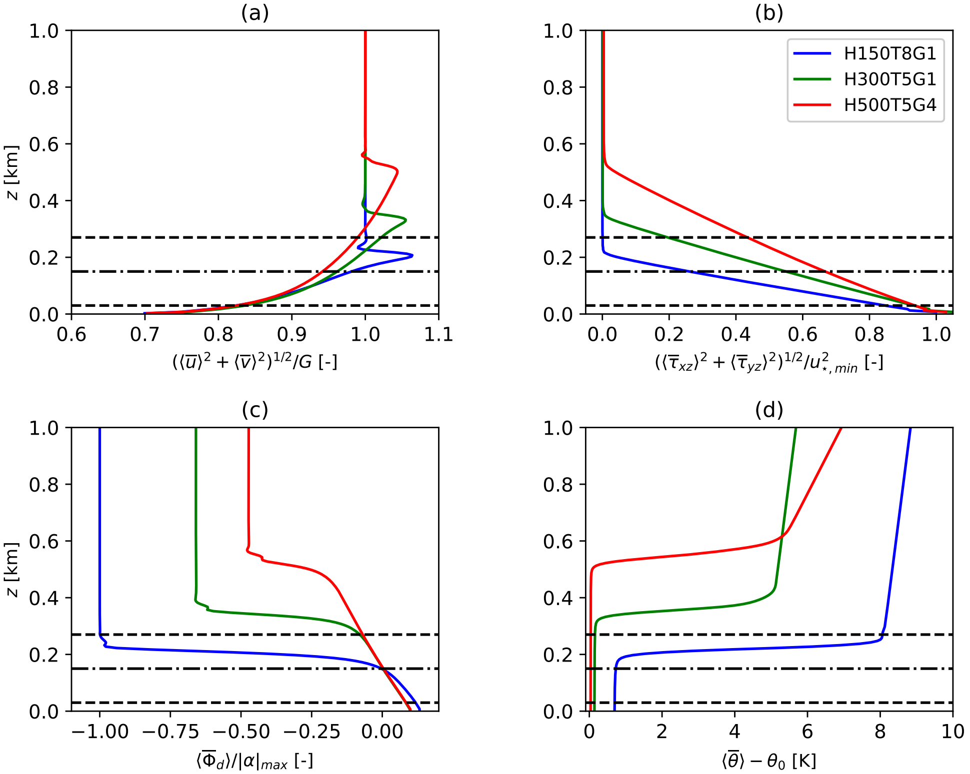

Figure 2. Vertical profiles of the velocity magnitude (a), the total shear stress (b), the wind direction (c) and the potential temperature (d). The space-averaged profiles are computed over the last 4 hours of simulations for the three sets of atmospheric conditions and normalized by $G = 10\,\mathrm{m\,s^{-1}}$, $u_{\star,\mathrm{min}} = 0.276\,\mathrm{m\,s^{-1}}$, $|\alpha|_{\mathrm{max}} = 18.55°$ and $\theta_0 = 288.15\,\mathrm{K}$, respectively . For all quantities, the top bar and the angle brackets represent time and horizontal averages, respectively.

Figure 2 shows the velocity (a) and the potential temperature profiles (d) averaged over the horizontal planes, together with the corresponding shear stress profiles (b) and wind directions (c). From Fig. 2 (a), it can be seen that the presence of the capping inversion limits the boundary-layer growth, so that the equilibrium inversion-layer height is attained when buoyancy forces balance the surface shear stress (Csanady, 1974). As observed by Lanzilao and Meyers (2024), the amplitude of the super-geostrophic jet that forms at the top of the ABL increases with decreasing inversion-layer heights. Above the jet, the shear stress profile reduces to zero (Fig. 2 (b)), the flow becomes laminar, and the velocity profile corresponds to the geostrophic wind. Figure 2 (d) shows that for the cases H150-$\Delta\theta$8-Γ1, H300-$\Delta\theta$5-Γ1, H500-$\Delta\theta$5-Γ4 the origin of the capping inversion moves to an altitude of 195 m, 325 m and 510 m, respectively, over the twenty-hour-long spin-up. We note that these values align with the predictions computed from Csanady (1974) (not detailed here). In the ABL, the Ekman spiral

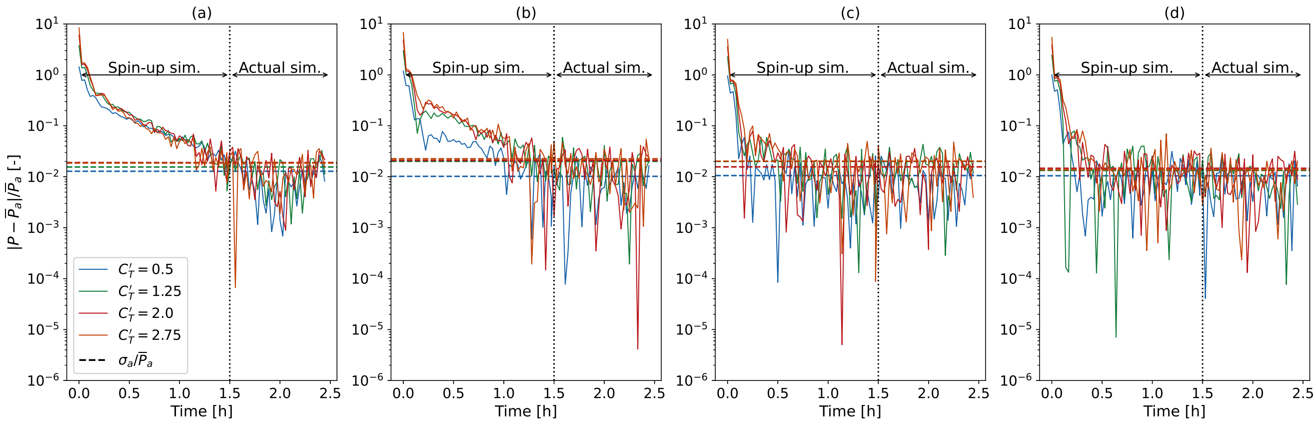

Figure 3. Evolution of the normalized power difference $|P - \overline{P}_a|$ measured during the two simulation phases for the four tested operating regimes and the four atmospheric conditions. Figures (a), (b), (c) and (d) correspond to conditions H150-$\Delta\theta$8-Γ1, H300-$\Delta\theta$5-Γ1, H500-$\Delta\theta$5-Γ4 and H500-$\Delta\theta$0-Γ0, respectively. For each of the sixteen considered cases, the threshold defined by $\sigma_a/\overline{P}_a$ is represented by the dotted line of the corresponding color. The quantities $\overline{P}_a$ and σ_a are the time-averaged power and corresponding standard deviation measured during the second phase only.

forms so that the wind-direction angle Φ_d, measured with respect to the axis perpendicular to the farm, varies with the altitude (Fig. 2 (c)). The angles Φ_d values in Fig. 2 (c) are normalized by the largest value of $|\alpha|$, where α is defined as the angle between the geostrophic wind and the velocity vector right above the ground. As reported by Allaerts and Meyers (2017) and Lanzilao and Meyers (2024), $|\alpha|$ is observed to be larger for lower capping inversions. Note that the wind-direction controller designed by Allaerts and Meyers (2015) is employed during the precursor phase to rotate the geostrophic wind so as to ensure no spanwise velocity components at hub height, i.e. $\Phi(z_{hub}) = 0°$. Finally, small oscillations of the velocity magnitude and the wind direction appear in the inversion layer (Fig. 2 (a,b)), as a result of the strong stratification that characterizes this region. This matter is addressed in Sullivan et al. (2016), where the authors show that eddies with a characteristic scale larger than the Doughtery–Ozmidov length are stratification-dependent. However, this length decreases as stratification increases, possibly leading to values of the Doughtery–Ozmidov length smaller than the grid spacing. Some of the Sub-grid scale eddies generated in the inversion-layer can be stratification dependent and can therefore not be accurately captured by the SGS model, causing the oscillations observed in Fig. 2 (a,b). Similar oscillations can be seen in e.g. Maas and Raasch (2022) and Pedersen et al. (2014).

3.2 Wind farm spin-up phase

The flow field generated at the last time step of the precursor phase is tiled over the concurrent-precursor domain and over the main domain described in Sec. 2.4. Then, we place the wind farm introduced in Sec. 2.5 in the main domain and we advance the simulation in time so that the flow adapts to the presence of the farm. Simultaneously, the concurrent-precursor flow evolves and is imposed in the fringe region following the methodology detailed in Sec. 2.3.

In the current work, we focus on obtaining accurate power estimations for a limited number of test cases. Therefore, first we check the convergence of the farm power. In Fig. 3, the evolution of the instantaneous wind farm power calculated over the two simulation phases is represented for all the considered conditions. We show the normalized difference with respect to the time-averaged power $\overline{P}_a$ obtained in the second phase only, i.e. the last 60 minutes depicted in Fig. 3. From this same phase, we retrieve the standard deviation of P_a for each set of atmospheric conditions and operating conditions. This quantity is denoted σ_a and is represented in Fig. 3 to assess convergence. For all the considered cases, the normalized deviation $\sigma_a/\overline{P}_a$ is of the order of 10^{-2}, and appears to slightly increase with C_T'.

Figure 3 shows that, beyond 90 minutes, any remaining trend appears to be of the order of the power fluctuations, for all the operating regimes and the atmospheric conditions. Interestingly, we note that the statistically steady-state is attained more rapidly for low-blockage conditions. Nevertheless, we retain a spin-up duration of 90 minutes, after which the final phase of the simulation is performed over one hour. The power and flow quantities are measured during this last phase, referred to as the actual simulation. Similar to the precursor phase (Sec. 3.1), the wind-direction controller of Allaerts and Meyers (2015) is employed during the wind farm spin-up phase. This controller is disabled in the actual simulation, however. Eventually, the same procedure is applied to the corresponding single wind turbine cases over the small domain, as discussed in Sec. 2.4.

4 Results

The results of the one-hour long actual simulations are discussed in this section. First, we provide an insight of the velocity fields in Sec. 4.1, pointing out the importance of the farm-induced effects. The corresponding power estimations are then analyzed in Sec. 4.2 to assess the potential of the collective axial-induction operational strategy.

4.1 Comparison of the farm-scale velocity fields

The instantaneous streamwise velocity field is provided in Fig. 4 for the four tested atmospheric conditions and the four operating regimes introduced in Sec. 2.5. Comparing cases with identical disc-based thrust coefficient (C_T'), the flow appears to significantly vary with the atmospheric conditions. This observation stresses the need to account for the potential temperature profile in the design of an efficient large-scale operating strategy. In particular, a large blockage effect is visible in the form of a bow-wave in Fig. 4 (a–d). Even though this effect was anticipated due to the low and strong capping inversion above the farm, we observe a significant decrease in amplitude of this feature when C_T' is decreased. The same pattern can be seen, though to a lesser extent, in the case H300-$\Delta\theta$5-Γ1 Fig. 4 (e–h). Under the set of conditions H500-$\Delta\theta$5-Γ4 (Fig. 4 (i–l)), large-scale effects are minor but become apparent when compared to the case H500-$\Delta\theta$0-Γ0 (Fig. 4 (m–p)). In particular, analyzing Fig. 4 (l) and Fig. 4 (p) together, we observe a slight velocity decrease limited to the front of the farm in Fig. 4 (l). Moreover, Fig. 4 (p) shows a stronger farm wake compared to Fig. 4 (l), providing evidence that a favorable pressure gradient still forms in situations where the capping inversion is high.

Eventually, observations of the vertical velocity field provided further evidence of the development of wind-farm-induced effects (not shown). In all the considered cases, the displacement of the capping inversion was seen to trigger internal gravity

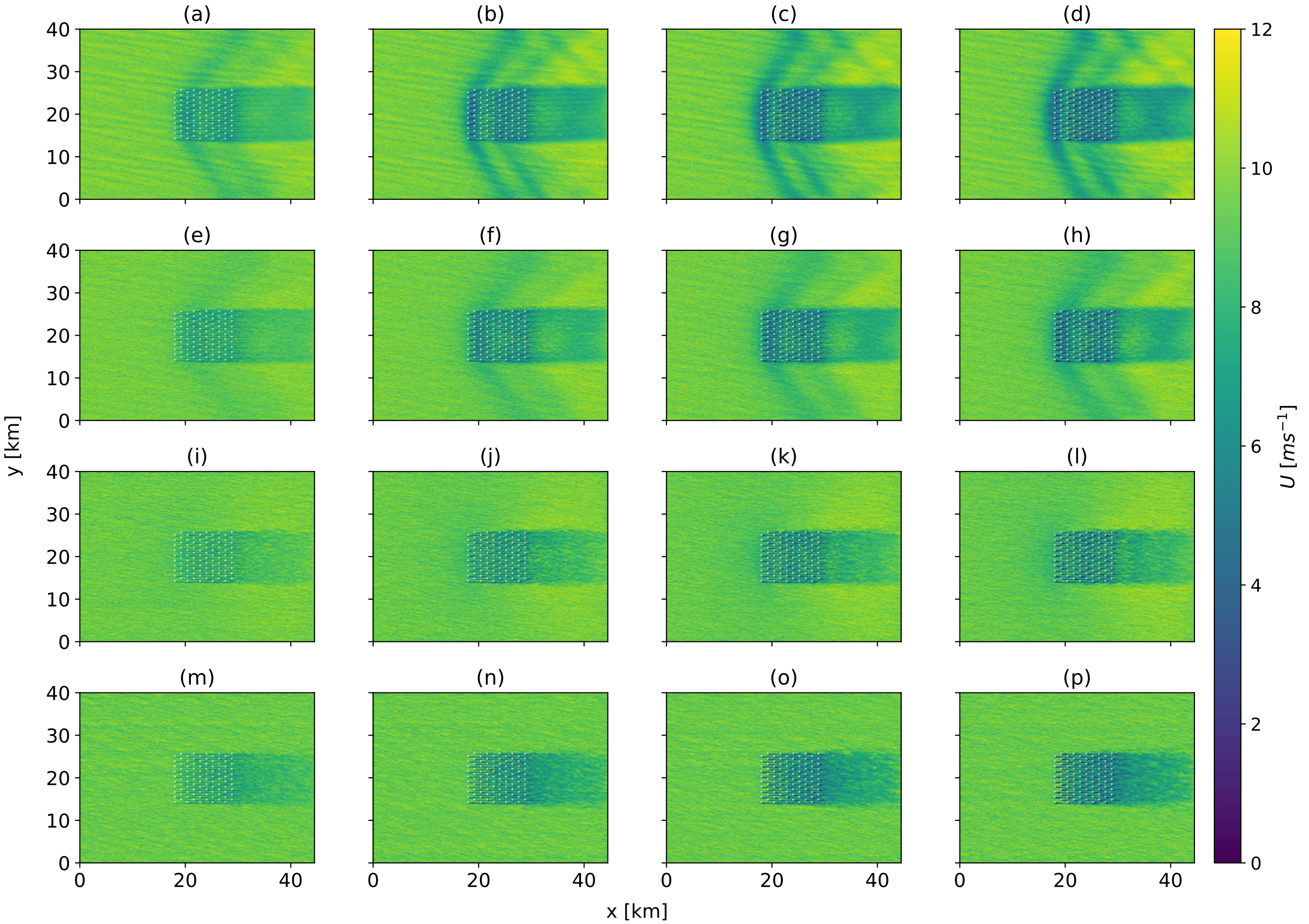

Figure 4. Instantaneous streamwise velocity field at hub height for the cases H150-$\Delta\theta$8-Γ1 (a–d), H300-$\Delta\theta$5-Γ1 (e–h), H500-$\Delta\theta$5-Γ4 (i–l) and H500-$\Delta\theta$0-Γ0 (m–p). Four operating regimes are considered: $C_T' = 0.50$ (a, e, i), $C_T' = 1.25$ (b, f, j), $C_T' = 2.0$ (c, g, k) and $C_T' = 2.75$ (d, h, l). The white markers indicate the turbine locations.

waves, yet to different degrees depending on the value of C_T'. Thus, stronger and weaker waves were observed for the cases where the farm operates at high and low C_T' values, respectively. We refer to Lanzilao and Meyers (2024) for a further-detailed analysis of this phenomenon.

4.2 Momentum extraction distribution across the farm

In order to assess the intensity of the thrust force exerted by the k^{th} turbine on the flow and its corresponding power, we define the time-averaged thrust and power coefficients (denoted $C_{T,k}$ and $C_{P,k}$, respectively) as follows:

$$C_{T,k} = \frac{\overline{F}_k}{\frac{1}{2}\rho_0 A \overline{U}_\infty^2} \quad \text{and} \quad C_{P,k} = \frac{\overline{P}_k}{\frac{1}{2}\rho_0 A \overline{U}_\infty^3}. \tag{8}$$

In these expressions, $A = \pi D^2/4$ is the disc area and $\overline{F}_k$ and $\overline{P}_k$ are the time-averaged turbine thrust (Eq. 5) and power (Eq. 7), respectively. Further, U_∞ is the reference wind speed computed as the streamwise velocity averaged over a layer of thickness D spanning the disc-precursor domain, i.e. the region defined by $[0, L_x^p] \times [0, L_y^p] \times [z_H - D/2, z_H + D/2]$. Within this region, we use a vertically dependent weighted average where the weights are given by the actuator disc chord length, i.e., the straight-line distance across the intersection of the disc and the horizontal plane at the considered altitude. For the cases H150-$\Delta\theta$8-Γ1, H300-Δ5-Γ1, H500-$\Delta\theta$5-Γ4 and H500-$\Delta\theta$0-Γ0, the reference speeds averaged over the last 4 hours of the precursor simulation are equal to $\overline{U}_\infty = 9.61\,\mathrm{m\,s^{-1}}$, $9.55\,\mathrm{m\,s^{-1}}$, $9.35\,\mathrm{m\,s^{-1}}$ and $9.35\,\mathrm{m\,s^{-1}}$, respectively. We note that the two expressions in Eq. 8 can be re-written as $C_{T,k} = C_T'(\overline{u}_{d,k}/\overline{U}_\infty)^2$ and $C_{P,k} = C_T'(\overline{u}_{d,k}/\overline{U}_\infty)^3$ using Eq. 5 and Eq. 7, with $\overline{u}_{d,k}$ the time average of $u_{d,k}$. The time-averaged thrust ($C_{T,sgl}$) and power ($C_{P,sgl}$) coefficients in the single turbine case are defined with respect to the corresponding thrust ($\overline{F}_{sgl}$) and power ($\overline{P}_{sgl}$), analogously to Eq. 8.

The distribution of the local thrust coefficient ($C_{T,k}$) over the farm is normalized by that of the single turbine ($C_{T,sgl}$) under the same operating conditions, and represented in Fig. 5. Therefore, Fig. 5 illustrates the momentum extracted by each turbine in the farm, compared to that of an isolated turbine. Because the disc-based thrust coefficient is common to each turbine in the farm, the ratio shown in Fig. 5 re-writes $C_{T,k}/C_{T,sgl} = \overline{F}_k/\overline{F}_{sgl} = (\overline{u}_{d,k}/\overline{u}_{d,sgl})^2$. When operating at $C_T' = 0.5$ (Fig. 5 (a,e,i,m)), wake interference between the turbines dominates, which results in a region of higher thrust values over the first two rows of turbines, followed by a quasi-uniform distribution across the rest of the farm. In the absence of a capping-inversion, the same conclusion applies regardless of the considered C_T' value (Fig. 5 (m,n,o,p)). For the CNBL conditions, the bow-wave pattern described in Fig. 4 is associated with a favorable pressure gradient that is for example visualized through thrust coefficients greater at the fourth than at the third row in the case H150-$\Delta\theta$8-Γ1 (Fig. 5 (a)). As C_T' increases, the velocity at the farm entry decreases so that the row of minimal thrust coefficient is shifted towards the front of the farm (Fig. 4 (d)). Interestingly, Fig. 5 (i–l) show that for a high capping inversion, blockage essentially affects the first two rows. Consequently, it is possible to select the value of C_T' common to all turbines so that the front-localized blockage and the wake effects downstream lead to a close-to-uniform thrust distribution across the farm (Fig. 5 (l)). More generally, provided that the operating regime can be set independently for each row of turbine, Fig. 5 indicates that the thrust distribution could be homogenized by either increasing or decreasing C_T' at the front of the farm subject to high-blockage (e.g., Fig. 5 (d)) or low-blockage conditions (e.g., Fig. 5 (i)), respectively.

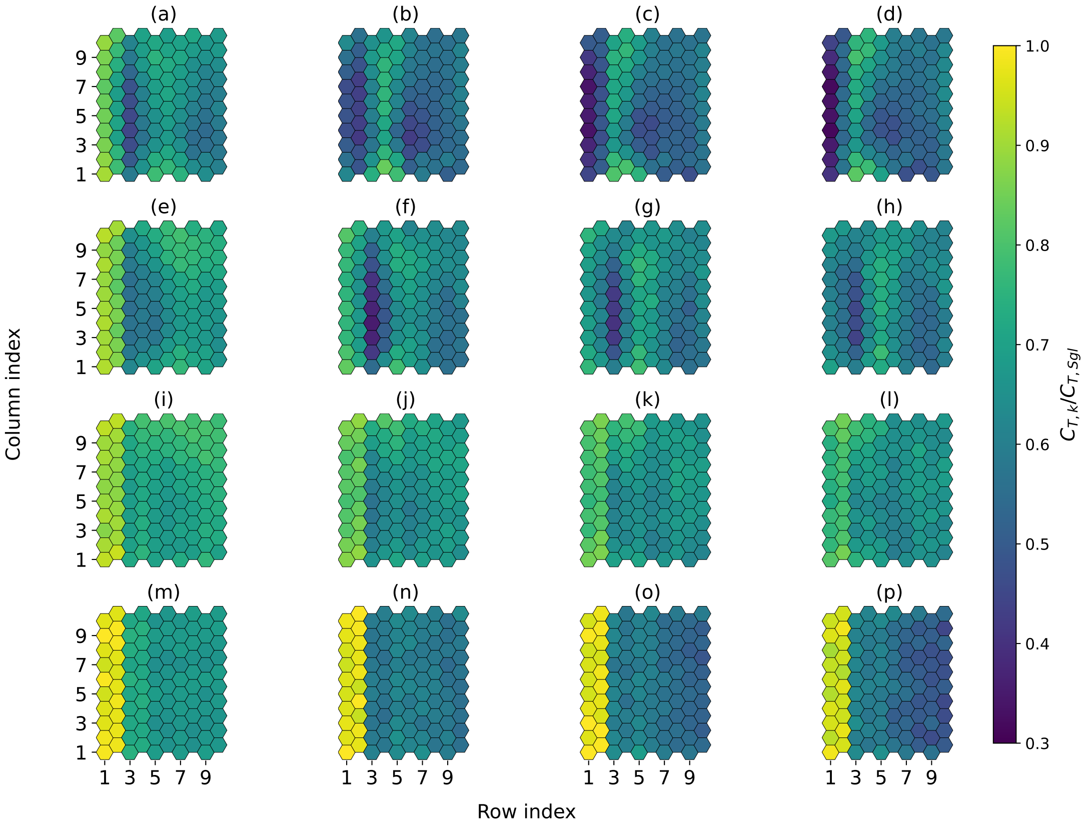

Figure 5. Distribution over the farm of the local thrust coefficient (Eq. 8) normalized by the corresponding single turbine thrust coefficient. The four atmospheric conditions, H150-$\Delta\theta$8-Γ1 (a–d), H300-$\Delta\theta$5-Γ1 (e–h), H500-$\Delta\theta$5-Γ4 (i–l) and H500-$\Delta\theta$0-Γ0 (m–p) are considered, together with the four operating regimes, $C_T' = 0.50$ (a, e, i, m), $C_T' = 1.25$ (b, f, j, n), $C_T' = 2.0$ (c, g, k, o) and $C_T' = 2.75$ (d, h, l, p).

4.3 Wind farm thrust and power coefficient curves

We define the wind farm thrust and power coefficients, denoted $C_{T,f}$ and $C_{P,f}$ respectively, as the average values of $C_{T,k}$ and $C_{P,k}$ over all the turbines in the farm. Combining Eq. 5 and Eq. 7 to Eq. 8, the farm thrust and power coefficients are thus expressed as:

320 $$C_{T,f} = \frac{\sum_k^{N_t} \overline{u}_{d,k}^2}{N_t \overline{U}_\infty^2} C_T' \quad \text{and} \quad C_{P,f} = \frac{\sum_k^{N_t} \overline{u}_{d,k}^3}{N_t \overline{U}_\infty^3} C_T' \tag{9}$$

The analysis is further enriched by considering the farm efficiency η_f, which can be written in the form of a product of the non-local and the wake efficiencies, denoted η_{nl} and η_w, respectively (Allaerts and Meyers, 2018). We therefore write

$$\eta_f = \eta_{nl}\,\eta_w, \quad \eta_{nl} = \frac{\overline{P}_1}{\overline{P}_\infty}, \quad \eta_w = \frac{\overline{P}_a}{N_t\,\overline{P}_1}, \tag{10}$$

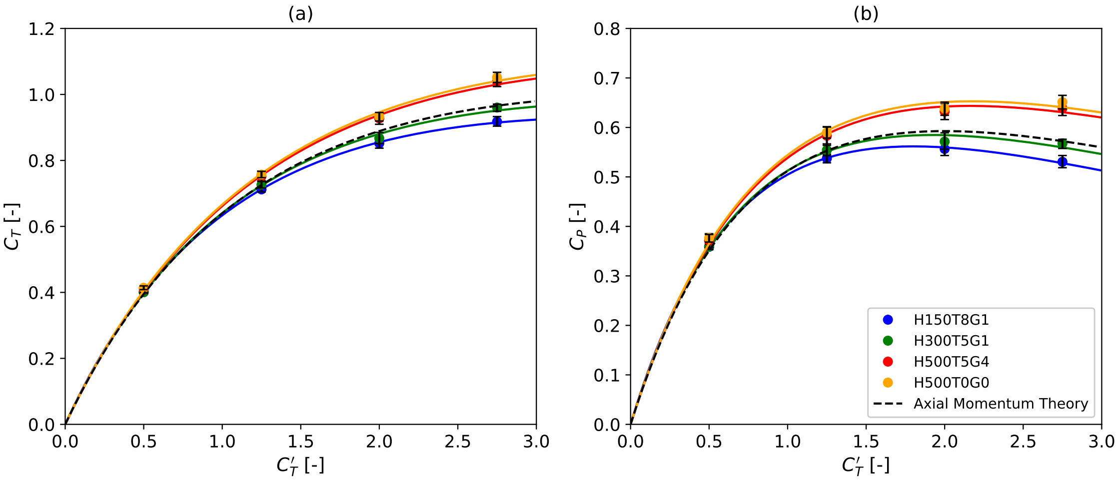

Figure 6. Thrust coefficients (a) and power coefficients (b) as a function of their disc-based counterparts for the stand-alone wind turbine. The results obtained under the four sets of atmospheric conditions are compared to the predictions of axial momentum theory. The 95% confidence intervals obtained with the moving-block bootstrap method are shown in black.

where $\overline{P}_a$ is the total farm power measured during the actual simulation and N_t the number of turbines in the farm. The notation $\overline{P}_1$ refers to the power per turbine, averaged over the most upstream row in the farm. Finally, $\overline{P}_\infty$ is the power of the turbine operating in isolation. All the quantities in Eq. 10 are time-averaged over the one-hour long simulations.

In Fig. 6, we show the thrust coefficients and the power coefficients of an isolated turbine computed following Eq. 8. The results are compared to the expressions,

$$C_T = \frac{16\,C'_T}{(C'_T+4)^2} \quad \text{and} \quad C_P = \frac{64\,C'_T}{(C'_T+4)^3}, \tag{11}$$

obtained from axial momentum theory (AMT) (Allaerts, 2016). Given the time-dependent nature of the thrust and power values collected with a sampling period $T_s = 100\,\mathrm{s}$, the time averages and the 95% confidence intervals shown in Fig. 6 are computed over the one-hour-long actual simulations using a moving block bootstrap method. We follow the procedure described by Bon and Meyers (2022) with overlapping blocks consisting of $n_b = 3$ samples over a total of $B = 1000$ bootstrap iterations. We performed a sensitivity study, not discussed here, to motivate the selected values for n_b and B.

As anticipated, the LES results exhibit the same behaviour as the theoretical predictions (Eq. 11), in particular at low operating regimes for which close agreement is observed in Fig. 6 (a) and Fig. 6 (b). Above $C'_T = 1.25$, the LES values significantly deviate from the AMT for the cases H150-$\Delta\theta$8-Γ1 and H500-$\Delta\theta$5-Γ4, showing under-prediction and over-prediction, respectively. Plausible causes of the deviations with respect to the classical axial momentum theory include the presence of shear, veer and turbulence in the simulations. It is however unclear whether the over-prediction obtained in the case H500-$\Delta\theta$5-Γ4 has a physical explanation. In Shapiro et al. (2019), the authors report that the velocity correction factor leads to slight over-estimations at large disc-based thrust coefficients. For instance, we observe a difference of 7% at $C'_T = 2.0$ in the present

Table 3. Values of the three fitting parameters of the single turbine thrust and power coefficient curves in Fig. 6.

Case	α_p	α_t	β
H150-$\Delta\theta$8-Γ1	67.3605	16.5490	1.1104
H300-$\Delta\theta$5-Γ1	65.5639	16.2539	1.0382
H500-$\Delta\theta$5-Γ4	64.3789	16.0565	0.9263
H500-$\Delta\theta$0-Γ0	64.7523	16.1153	0.9184

study (Fig. 6 (b)), which aligns with the discrepancy of the order of 5% retrieved from the results of Shapiro et al. (2019) at the same C_T' value. Moreover, we emphasize that the expression of the velocity correction factor was obtained for a uniform flow (Shapiro et al., 2019), therefore possibly resulting in larger discrepancies with respect to the AMT when employed in a non-uniform flow. As a matter of fact, the over-prediction between the AMT and the results of an uniform-flow simulation performed at $C_T' = 1.44$ was found to be about half that observed with the case H500-$\Delta\theta$5-Γ4 (not shown). The validity of the velocity correction factor employed with non-uniform profiles could be the topic of future works. The results of LES simulations relying on a higher fidelity turbine representation, e.g. Actuator Line Model, should be used as a reference.

In Fig. 6 (a) and Fig. 6 (b), we introduce a simple heuristic fit in which the parameters α_t, α_p and β of the laws

$$C_T = \alpha_t \, C_T' / (\beta \, C_T' + 4)^2 \quad \text{and} \quad C_P = \alpha_p \, C_T' / (\beta \, C_T' + 4)^3 \tag{12}$$

are fitted to the LES data points using the least squares method. As the two relations in Eq. 12 share a common parameter β, the procedure results in a simple joint-optimization problem between the eight LES data points corresponding to the four tested C_T' values. The optimized value of each of the three parameters is given in Table 3. In Eq. 12, an increasing number of parameters was introduced and a convergence analysis on the residual of the least squares method then motivated the choice of α_t, α_p and β. Physically, we postulate that the three parameters allow to account for the impact of shear, veer and turbulence, disregarded in the classical AMT.

At the wind farm scale, we compute the thrust and power coefficients, $C_{T,f}$ and $C_{P,f}$, following Eq. 9. Similarly to the single wind turbine case, we employ the moving block bootstrapping method. However, because the confidence intervals do not exceed $\pm 1\%$, only the time-averaged values of $C_{T,f}$ and $C_{P,f}$ are represented in Fig. 7. The corresponding curves are fitted using laws of the form

$$C_{T,f} = \alpha_{t,f} \, C_T' / (C_T' + \delta_{t,f})^{\gamma_{t,f}} \quad \text{and} \quad C_{P,f} = \alpha_{p,f} \, C_T' / (C_T' + \delta_{p,f})^{\gamma_{p,f}}, \tag{13}$$

where six degrees of freedom are introduced in total. In Eq. 13, the two sets of three fitting parameters are determined for $C_{T,f}$ and $C_{P,f}$ through two independent least squares methods. Each of the two fitting therefore sets the values of three parameters using four LES points. The corresponding values are tabulated in Table 4. We initially explored other options, e.g. using only three parameters to approximate $C_{T,f}$ and $C_{P,f}$ as in the single turbine case. However, this led to large fitting errors in all the tested cases.

Table 4. Values of the six fitting parameters of the wind farm thrust and power coefficient curves in Fig. 7.

Case	$\alpha_{t,f}$	$\delta_{t,f}$	$\gamma_{t,f}$	$\alpha_{p,f}$	$\delta_{p,f}$	$\gamma_{p,f}$
H150-$\Delta\theta$8-Γ1	0.5586	0.5482	0.9080	0.4158	0.5383	1.3484
H300-$\Delta\theta$5-Γ1	0.7506	0.8190	0.9820	0.6655	0.8288	1.4803
H500-$\Delta\theta$5-Γ4	0.9983	1.0969	1.0040	0.9929	1.0885	1.4982
H500-$\Delta\theta$0-Γ0	0.9222	1.0041	1.0113	0.9054	1.0181	1.5057

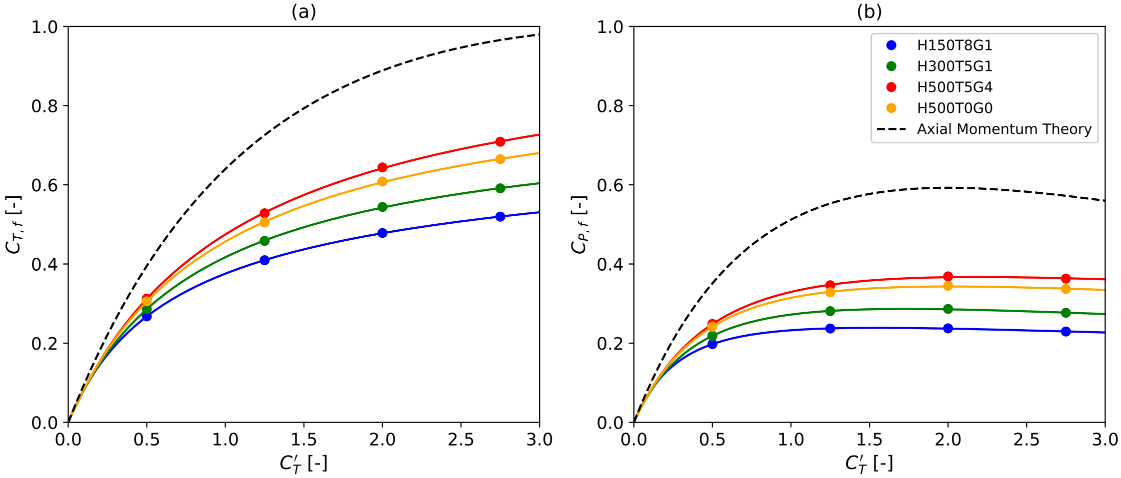

Figure 7. Wind farm thrust coefficients (a) and power coefficients (b) as a function of their disc-based counterparts. The results obtained under the four sets of atmospheric conditions are compared to the predictions of the Axial Momentum Theory for a single turbine.

The wind farm thrust and power coefficient curves shown in Fig. 7 can be discussed in parallel to the efficiency curves obtained from Eq. 10 and represented in Fig. 8. First, in Fig. 7 (b), we notice that the evolution of $C_{P,f}$ with C'_T is much flatter than in the single wind turbine situation (Fig. 6 (b)). In Fig. 8 (c), the farm efficiency is essentially constant above $C'_T \simeq 1.25$ in the three CNBL cases. This results in a region of nearly constant $C_{P,f}$ values, the maximum of which is offset towards C'_T values lower than in the stand-alone configuration (Fig. 6 (b)). In the remainder of this analysis, the maximum power coefficient and the corresponding C'_T and $C_{T,f}$ are denoted $C^{\star}_{P,f}$, $C'^{\star}_T$ and $C^{\star}_{T,f}$, respectively.

Moreover, the inspection of Fig. 8 (a) reveals that the ability of the turbines to generate more power by increasing C'_T towards its Betz optimal value ($C'_T = 2$) is considerably harmed by the inevitable blockage effect that accompanies large C'_T values. This phenomenon appears to be clearly amplified for inflows with a low capping inversion (H150-$\Delta\theta$8-Γ1). On the contrary, the non-local efficiency remains constant with respect to C'_T in the absence of a capping inversion (case H500-$\Delta\theta$0-Γ0). Under CNBL conditions, we notice in Fig. 8 (b) that the wake efficiency is a growing function of C'_T that reaches values significantly greater than one under specific conditions. This observation is explained by the physical meaning of η_w, which should be

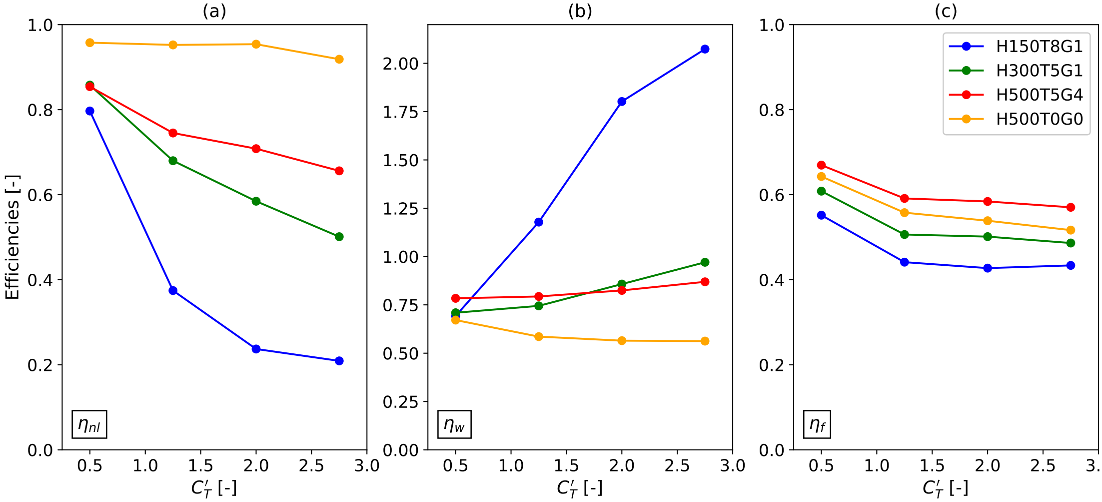

Figure 8. Non-local (a), wake (b) and global wind farm (c) efficiencies computed from Eq. 10 for all the operating points under the four sets of atmospheric conditions. The vertical axis in (b) is extended for the sake of readability.

interpreted as the ratio between the performances of the farm and that of the first row. Consequently, the values $\eta_w > 1$ in Fig. 8 (b) correspond to cases where the downstream rows, although waked, extract more power than the first one. This is explained by a large pressure increase before the first row, followed by a favorable pressure gradient that accelerates the flow deeper into the farm, as previously visualized in Fig. 4. Under the atmospheric conditions H500-$\Delta\theta$5-Γ4, the favorable pressure gradient leads to values of the farm efficiency larger than in the corresponding TNBL case (H500-$\Delta\theta$0-Γ0), as indicated in Fig. 8 (c). Similar observations are reported in Lanzilao and Meyers (2024)

Below $C_T' \simeq 1.25$, the farm poses so little resistance to the flow that only minor blockage effects occur. Simultaneously, we note that this range of operating regimes exhibits high sensitivity to blockage. This is visible in Fig. 8 (a), where the non-local efficiencies of the case H150-$\Delta\theta$5-Γ1 is initially close to that of the cases H300-$\Delta\theta$5-Γ1 and H500-$\Delta\theta$5-Γ4 but drastically decreases as C_T' increases. This results in a slightly higher farm efficiency at low C_T' values (Fig. 8 (c)), in turn causing the shifting of the curve maximum towards the left in Fig. 7.

Eventually, Fig. 7 (a) shows a strong decrease of the farm thrust coefficient values when compared to those of the isolated turbine (Fig. 6 (a)). However, each wind farm thrust coefficient curve remains much steeper than its power counterpart (Fig. 7), supporting the idea that load can be effectively reduced with only a limited impact on power.

4.4 Performance assessment of the collective axial-induction strategy

In this section, the trade-off between thrust and power is explicitly shown in Fig. 9 (a) by plotting the information of Fig. 7 (a,b) in the $C_{P,f} - C_{T,f}$ coordinate system. Fig. 9 (c) is obtained by applying the same procedure to the results of the single turbine

Table 5. Operating parameters selected in the first approach and corresponding gains with respect to the classical operating point for the four atmospheric conditions. The disc-based thrust coefficient is set to $C_T'^{\star}$ to maximize power extraction.

	H150-$\Delta\theta$8-Γ1	H300-$\Delta\theta$5-Γ1	H500-$\Delta\theta$5-Γ4	H500-$\Delta\theta$0-Γ0
$C_T'^{\star}$ [-]	1.55	1.73	2.18	2.01
$C_{P,f}^{\star}$ [-]	0.24	0.29	0.37	0.34
$C_{T,f}^{\star}$ [-]	0.44	0.52	0.66	0.61
ε_P [%]	0.83	0.35	0.13	0.001
ε_T [%]	-7.64	-4.59	3.07	0.22

simulations (Fig. 6 (a,b)). Then, all the curves in both Fig. 9 (a) and Fig. 9 (c) are normalized by their peak value and represented in Fig. 9 (b) and Fig. 9 (d), respectively. In Fig. 9 (d), the normalized curves collapse into the AMT law as this choice of normalization can be shown to be independent of the fitting parameters introduced in Eq. 12. By contrast, we note a clear deviation of the normalized wind farm curves from the predictions of the AMT in Fig. 9 (b). This observation emphasizes that large-scale effects substantially impact the trade-off between thrust and power and therefore influence the design of the farm operating point. In Fig. 9 (a), the three curves corresponding to CNBL conditions are affected by both blockage effects and wake interactions. On the contrary, the curve obtained for the case H500-$\Delta\theta$0-Γ0 accounts for wake effects only, and can thus be considered a blockage-free reference. For each of the curves generated under CNBL conditions in Fig. 9 (a), we conclude that the deviation observed with respect to the TNBL reference case results from blockage effects.

We now focus on the design of a wind farm operating point that accounts for large-scale effects. To this end, we explore three potential wind farm set points and evaluate the corresponding thrust and power variation with respect to the standard operating regime $C_T' = 2$. For the sake of clarity, we denote by $\hat{C}_{T,f}$ and $\hat{C}_{P,f}$, respectively, the coefficients $C_{T,f}$ and $C_{P,f}$ evaluated at $C_T' = 2$. Further, we define the relative thrust and power difference with respect to the standard regime as $\varepsilon_T = (C_{T,f} - \hat{C}_{T,f})/\hat{C}_{T,f}$ and $\varepsilon_P = (C_{P,f} - \hat{C}_{P,f})/\hat{C}_{P,f}$.

The first method consists in operating each turbine in the farm at $C_T'^{\star}$, so that the peak of the farm power coefficient curve, i.e. $C_{P,f}^{\star}$, is achieved. This operating regime is denoted by a black star in Fig. 9 (a). An alternative that could be of interest is allowing for a decrease of $C_{P,f}$ compared to the standard operating regime $C_T' = 2$ (Betz limit). With the second approach, we consider for instance a decrease of 1% in $C_{P,f}$. This choice, although somewhat arbitrary, aligns with the reduction in power observed when an isolated IEA 15 MW turbine operates at the design thrust set point, prioritizing load mitigation over maximizing power output (Gaertner et al., 2020). From the three fitted curves shown in Fig. 9 (a), we retrieve the $C_{T,f}$ value at which 99% of $\hat{C}_{P,f}$ is achieved in each case and we denote it $C_{T,f}^{\times}$. We refer to the corresponding farm power coefficient as $C_{P,f}^{\times}$ and we denote the disc-based thrust coefficient by $C_T'^{\times}$. Last, the third method further explores the potential for thrust reduction by allowing for a power decrease of 10%. Similarly to the second approach, $C_{T,f}^{\blacklozenge}$ is the farm coefficient at which 90% of $\hat{C}_{P,f}$ is achieved. The corresponding farm power coefficient and disc-based thrust coefficient are $C_{P,f}^{\blacklozenge}$ and $C_T'^{\blacklozenge}$, respectively. The three tested farm operating points and the corresponding gains obtained under each atmospheric condition are listed in Table 5, Table 6 and Table 7.

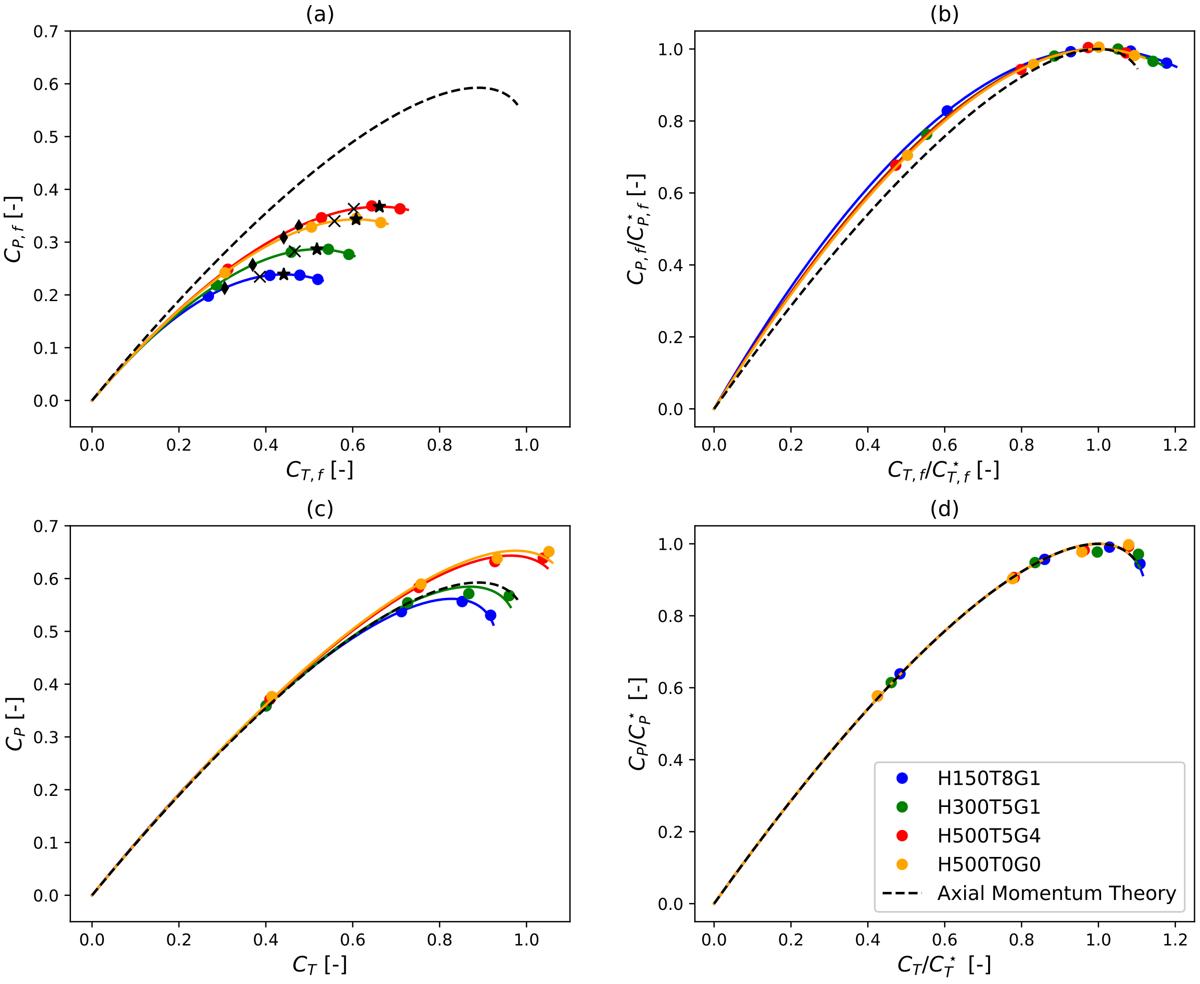

Figure 9. (a) Wind farm power coefficient as a function of the wind farm thrust coefficient. For each of the four sets of conditions, the tested operating points $(C^{\star}_{T,f}, C^{\star}_{P,f})$, $(C^{\times}_{T,f}, C^{\times}_{P,f})$ and $(C^{\blacklozenge}_{T,f}, C^{\blacklozenge}_{P,f})$ are indicated with star, cross and diamond symbols, respectively. (b) Identical as (a) but the maximum farm power coefficient and corresponding thrust coefficient are used to normalize the curve under each condition. (c) Single turbine power coefficient as a function of the thrust coefficient for each condition. (d) Identical to (c) but the maximum power coefficient and corresponding thrust coefficient are used to normalize the curve under each condition.

In Table 5, we show that operating the farm at $C'^{\star}_T$ to maximize power extraction leads to very slight power increments. This is the case, however, provided that the blockage effect is strong enough, i.e. H150-$\Delta\theta 8$-$\Gamma 1$ and H300-$\Delta\theta 5$-$\Gamma 1$. More interestingly, we observe for those two cases that the power increase, although minor, is associated with a load reduction of the order of 5%. In the absence of blockage (H500-$\Delta\theta 0$-$\Gamma 0$), the deviation from the standard regime is negligible, indicating

Table 6. Operating parameters selected in the second approach and corresponding gains with respect to the classical operating point for the four atmospheric conditions. The disc-based thrust coefficient is set to $C_T'^{\times}$ so that 99% of $\hat{C}_{P,f}$ is achieved.

	H150-$\Delta\theta$8-Γ1	H300-$\Delta\theta$5-Γ1	H500-$\Delta\theta$5-Γ4	H500-$\Delta\theta$0-Γ0
$C_T'^{\times}$ [-]	1.07	1.30	1.69	1.58
$C_{P,f}^{\times}$ [-]	0.23	0.28	0.36	0.34
$C_{T,f}^{\times}$ [-]	0.39	0.47	0.6	0.56
ε_P [%]	-1.0	-1.0	-1.0	-1.0
ε_T [%]	-19.16	-14.01	-6.1	-7.98

Table 7. Operating parameters selected in the third approach and corresponding gains with respect to the classical operating point for the four atmospheric conditions. The disc-based thrust coefficient is set to $C_T'^{\blacklozenge}$ so that 90% of $\hat{C}_{P,f}$ is achieved.

	H150-$\Delta\theta$8-Γ1	H300-$\Delta\theta$5-Γ1	H500-$\Delta\theta$5-Γ4	H500-$\Delta\theta$0-Γ0
$C_T'^{\blacklozenge}$ [-]	0.64	0.78	1.01	0.93
$C_{P,f}^{\blacklozenge}$ [-]	0.21	0.26	0.33	0.31
$C_{T,f}^{\blacklozenge}$ [-]	0.31	0.37	0.48	0.44
ε_P [%]	-10.0	-10.0	-10.0	-10
ε_T [%]	-36.11	-31.84	-25.81	-27.25

that the total power is maximized when each turbine operates at the Betz limit. We anticipate this to be no longer the case in a situation where the C_T' distribution can be set non-homogeneously across the farm to mitigate the wake effects of the upstream turbines. The results obtained with the second operational strategy are listed in Table 6. From this table, we conclude that substantial load reduction can be achieved at the expense of a minor power loss. In particular, the wind farm thrust coefficients in Table 6 are observed to decrease by up to 19% under significant blockage. For the same atmospheric conditions, the results of the third approach tabulated in Table. 7 indicate a load reduction of 36%. This decrease is limited to 25% for the case H500-$\Delta\theta$5-Γ4, however.

As a conclusion, we show that axial-induction strategies for load reduction are particularly effective for small power reductions relative to the classical operating regime, that is, in the region where the slope of the curves in Fig. 9 (a) is slight. We believe this constitutes an important finding, upon which more sophisticated wind farm operational strategies can be developed. In the future, investigating the sensitivity of the results to the turbine type, the farm layout or the free-stream velocity could be of interest. Regarding the ABL flow profile, we anticipate that the diameter-to-hub-height ratio and the ratio of the roughness length to the hub height are meaningful to the problem. We denote them $D^* = D/z_H$ and $z_0^* = z_0/z_H$, respectively. Further, we follow the expression of the similarity parameter $H^* = |f_c|H/u_*$ (Sood, 2023), where f_c is the Coriolis frequency, H is the boundary-layer height and u_* is the friction velocity. We note that the hub height velocity U_H can substitute u_*, using a log-law profile and the parameter z_0^* defined above. Throughout the present work, D^* and z_0^* were kept constant whereas different values of H^* were considered. We refer to, e.g. Csanady (1974), to relate H^* to the potential temperature parameters set in Sec. 2.5. Lastly, the present work provided evidence of the substantial impact of C'_T on the flow dynamics. More generally, we expect power density to play a crucial part in the design of an effective farm operating strategy. Therefore, we introduce the disc-based friction coefficient factor defined in Calaf et al. (2010) as the fourth non-dimensional number to account for power density. This ratio reads $c'_{ft} = \pi C'_T/(4S_xS_y)$, where S_x and S_y are the turbine spacings (expressed in number of diameters) in the streamwise and spanwise directions, respectively. As a result, similar effects on the total power extraction may be expected for similar values of c'_{ft}.

5 Conclusions

We investigated the potential of collective axial-induction operating strategies in large wind farms to mitigate the effects of blockage. For that purpose, a series of large-eddy simulations of a large farm of 100 15MW turbines placed in a staggered configuration were performed. Each turbine was represented by an actuator-disc with adjustable disc-based thrust coefficient. Overall, the study covered three different conventionally neutral boundary-layer conditions, for which little to strong blockage effects were expected. Additionally, a fourth set of atmospheric conditions was considered, representing a truly neutral boundary-layer. Alongside varying the flow conditions, the disc-based thrust coefficient of each turbine in the farm was successively set to four values, uniformly over the farm. Consequently, a total of sixteen simulations were carried out.

First, a precursor simulation was run for each of the three CNBL conditions, after which a spin-up simulation was performed for every operating regime. A convergence analysis on the farm power motivated the use of 90-minute-long spin-up phases. In each case, thrust and power measurements were subsequently collected over a one-hour-long simulation.

The streamwise velocity fields provided evidence of the significant meso-scale effects induced by the presence of the farm and shed light on the conditions that foster it. For low capping inversion cases, a low-velocity region was observed to develop upstream of the farm in the form of a bow wave. However, we showed that this blockage effect was significantly attenuated for low values of the disc-based thrust coefficients. Next, the analysis of the thrust distribution throughout the farm indicated strong heterogeneities caused by the simultaneous effects of wakes and blockage.

The results were then discussed in terms of the wind farm thrust and power coefficients, together with the wind farm, wake and non-local efficiencies. For all the tested CNBL conditions, the non-local efficiency decreased when increasing C'_T, with a significant drop observed for the case H150-$\Delta\theta 8$-$\Gamma 1$, particularly. For the same conditions, wake efficiencies greater than one further indicated the presence of a favorable pressure gradient throughout the farm. For values of the disc-based thrust coefficient larger than 1.25, the farm efficiency was found to be essentially constant with C'_T but strongly dependent on the atmospheric conditions. As a result, we observed a flattening of the farm power coefficient curve with respect to its single-turbine counterpart. Finally, we proposed three approaches to address thrust and power trade-offs. We found that operating the turbines below the optimal Betz point could simultaneously maximize power extraction and reduce the loading by more than 7% under strong blockage. We further concluded that enabling a 1% power reduction could result in a load decrease of 6% to 19%, depending on the conditions. The same factor was seen to reach between 25% and 36% at the expense of a power decrease of 10%, however.

In the future, we plan on expanding the study to other values of the capping inversion parameters. More generally, a similar analysis performed for stable and unstable boundary-layers profiles could be of interest. Finally, we intend to investigate the benefits of more advanced operational strategies, for instance by considering non-uniform C_T' distributions over the farm.

Appendix A: Detailed formulation of the governing equations

The set of equations described in Sec. 2.1 for the three-dimensional filtered velocity field (u_i) and the filtered potential temperature (θ) reads as follows:

$$\frac{\partial u_i}{\partial x_i} = 0 \tag{A1}$$

$$\frac{\partial u_i}{\partial t} + \frac{\partial}{\partial x_j}(u_j u_i) = f_c \epsilon_{ij3} u_j + \delta_{i3} g \frac{\theta - \theta_0}{\theta_0} - \frac{\partial \tau_{ij}^{sgs}}{\partial x_j} - \frac{1}{\rho_0}\frac{\partial p^*}{\partial x_i} - \frac{1}{\rho_0}\frac{\partial p_\infty}{\partial x_i} + f_i^{tot} \tag{A2}$$

$$\frac{\partial \theta}{\partial t} + \frac{\partial}{\partial x_j}(u_j \theta) = -\frac{\partial q_j^{sgs}}{\partial x_j}, \tag{A3}$$

where Eq. A1, A2 and A3 are the continuity, momentum and potential-temperature transport equations, respectively. Note that the streamwise, spanwise and vertical directions are indicated by the indices i = 1,2 and 3, respectively. In Eq. A2, the first term on the right-hand side accounts for the Coriolis force generated by the rotation of the earth at angular velocity Ω_E and latitude ϕ, where $f_c = 2\Omega_E \sin\phi$ is the Coriolis frequency and ϵ_{ij3} the Levi-Citiva symbol. Further, the buoyancy effect on the vertical momentum is represented by the second component in the RHS term of Eq. A2, where θ_0 denotes the reference potential temperature and δ_{i3} is the Kronecker delta. The effect of the subgrid-scale dynamics and heat transfer on the resolved flow is accounted for through the stress tensor τ_{ij}^{sgs} (Eq. A2) and the heat flux q_j^{sgs} (Eq. A3), respectively. In Eq. A2, the background pressure and the filtered fluctuations around it are denoted p_∞ and p^*. Eventually, the body force term f_i^{tot} is composed of the wind farm forcing on the flow (Eq. 6), the fringe-region forcing (Eq. B3) and the Rayleigh damping (Eq. B1).

Appendix B: Mathematical expressions of the Rayleigh-damping, the fringe forcing functions and the vertical momentum-damping factor

As introduced in Sec. 2.3, a Rayleigh-damping layer is used as the non-reflective upper boundary condition in the main domain. Along the three directions ($i = 1,2,3$) the corresponding forcing term per unit mass reads:

$$f_i^{\mathrm{ra}}(\mathbf{x}) = -\nu(z)\left(u_i(\mathbf{x}) - U_{g,i}\right), \tag{B1}$$

where $U_{g,i}$ is the component of the geostrophic wind G along the considered direction. The buffer intensity increases with height at a rate controlled by the Rayleigh function $\nu(z)$. Following Lanzilao and Meyers (2023), we write for $z > (L_z - L_z^{\mathrm{ra}})$:

$$\nu(z) = \breve{\nu}\left(1 - \cos\left(\frac{\pi}{s^{\mathrm{ra}}}\frac{z - (L_z - L_z^{\mathrm{ra}})}{L_z^{\mathrm{ra}}}\right)\right), \tag{B2}$$

with $\breve{\nu} = \nu^{\mathrm{ra}} N$ the amplitude parameter and N the Brunt-Väisälä frequency. The values of L_z^{ra}, ν^{ra} and s^{ra} (see Table. 1) are determined in light of the thorough analysis provided by Lanzilao and Meyers (2023) to minimize reflectivity.

Moreover, in Lanzilao and Meyers (2023), the authors express the forcing term related to the fringe-region as:

$$f_i^{\mathrm{fr}}(\mathbf{x}) = -h(x)\left(u_i(\mathbf{x}) - u_{prec,i}(\mathbf{x})\right), \tag{B3}$$

where $u_{prec,i}$ denotes the velocity field retrieved from the concurrent precursor simulation. To ensure that the forcing is gradually applied over the fringe-region, we employ the smooth function

$$h(x) = -h_{\max}\left(F\left(\frac{x - x_s^h}{\delta_s^h}\right) - F\left(\frac{x - x_e^h}{\delta_e^h} + 1\right)\right), \tag{B4}$$

where

$$F(x) = \begin{cases} 0, & \text{if } x \leq 0 \\ \frac{1}{1+\exp\left(\frac{1}{x-1}+\frac{1}{x}\right)} & \text{if } 0 < x < 1 \\ 1, & \text{if } x \geq 1. \end{cases} \tag{B5}$$

The values of the parameters x_s^h, x_e^h, δ_s^h, δ_e^h are given in Table. 2. Finally, Lanzilao and Meyers (2023) propose to locally damp the vertical momentum term in the fringe region so as to prevent the propagation of gravity waves triggered by the fringe forcing. The damping factor multiplies the vertical momentum convective term in Eq. A2 and is expressed as:

$$d(x,z) = 1 - \left(F\left(\frac{x - x_s^d}{\delta_s^d}\right) - F\left(\frac{x - x_e^d}{\delta_e^d} + 1\right)\right)\mathcal{H}(z - H), \tag{B6}$$

where the Heaviside function $\mathcal{H}$ ensures zero damping inside the ABL, i.e. up to H. The selected values of the parameters x_s^d, δ_s^d, x_e^d and δ_e^d in Eq. B6 are tabulated in Table. 2.

Author contributions. TD and JM jointly defined the methodology and the simulation set-ups. The simulations and post-processing steps were carried out by TD. TD and JM jointly wrote the manuscript.

Competing interests. At least one of the (co-)authors is a member of the editorial board of *Wind Energy Science*. The authors have no other competing interests to declare.

Acknowledgements. The authors gratefully acknowledge support from the Belgian Federal Public Planning Service Science Policy (BELSPO). The computational resources and service in this work were provided by the VSC (Flemish Supercomputer Center), funded by the Research Foundation Flanders (FWO) and the Flemish Government department EWI. The authors thank Luca Lanzilao for helpful discussions.

Financial support. Project ETREND, funded by the Belgian Federal Public Planning Service Science Policy (BELSPO) under the Brain-be 2.0 programme (Contract number B2/223/P1/E-TREND)

References

Allaerts, D.: Large-eddy simulation of wind farms in conventionally neutral and stable atmospheric boundary layers. PhD thesis, KULeuven, Leuven, Belgium, 2016.

Allaerts, D. and Meyers, J.: Large eddy simulation of a large wind-turbine array in a conventionally neutral atmospheric boundary layer, Phys. Fluids, 27, 2015.

Allaerts, D. and Meyers, J.: Boundary-layer development and gravity waves in conventionally neutral wind farms, J. Fluid Mech., 814, 95–130, 2017.

Allaerts, D. and Meyers, J.: Gravity waves and wind-farm efficiency in neutral and stable conditions, Bound.-lay. Meteorol., 166, 269–299, 2018.

Allaerts, D. and Meyers, J.: Sensitivity and feedback of wind-farm-induced gravity waves, J. Fluid Mech., 862, 990–1028, 2019.

Annoni, J., Fleming, P., Johnson, K., Bay, C., Taylor, T., and Pao, L.: Efficient Optimization of Large Wind Farms for Real-Time Control: Preprint, Golden, CO: National Renewable Energy Laboratory, 2017.

Bon, T. and Meyers, J.: Stable channel flow with spanwise heterogeneous surface temperature, J. Fluid Mech., 933, A57, 2022.

Bossanyi, E. and Bleeg, J.: How do wind farm blockage and axial-induction interact?, J. Phys.: Conf. Ser., 2767, 2024.

Calaf, M., Meneveau, C., and Meyers, J.: Large eddy simulation study of fully developed wind-turbine array boundary layers, Phys. Fluids, 22, 2010.

Canuto, C., Hussaini, M., Quarteroni, A., and Zang, T.: Spectral Methods in Fluid Dynamics, Springer, 1998.

Csanady, G.: Equilibrium theory of the planetary boundary layer with an inversion lid, Boundary-Layer Meteorology, 6, 63–79, 1974.

Delport, S.: Optimal control of a turbulent mixing layer. PhD thesis, KULeuven, Leuven, Belgium, 2010.

Fleming, P., Annoni, J., Shah, J. J., Wang, L., Ananthan, S., Zhang, Z., Hutchings, K., Wang, P., Chen, W., and Chen, L.: Field test of wake steering at an offshore wind farm, Wind Energ. Sci., 2, 229–239, 2017.

Gaertner, E., Rinker, J., Sethuraman, L., Zahle, F., and Anderson, B.: Definition of the IEA 15-Megawatt offshore reference wind, Golden, CO: National Renewable Energy Laboratory, 2020.

Gebraad, P.: Data-driven Wind Plant Control, Ph.D. Thesis, Delft University of Technology, Delft, The Netherlands, 2014.

Goit, J. and Meyers, J.: Optimal control of energy extraction in wind-farm boundary layers, J. Fluid Mech., 768, 2015.

González, J., Payán, M., Santos, J., and Gonzalez, A.: Maximizing the overall production of wind farms by setting the individual operating point of wind turbines, Renew. Energ., 80, 2015.

Lanzilao, L. and Meyers, J.: Set-point optimization in wind farms to mitigate effects of flow blockage induced by atmospheric gravity waves, Wind Energ. Sci., 6, 2021.

Lanzilao, L. and Meyers, J.: Effects of self-induced gravity waves on finite wind-farm operations using a large-eddy simulation framework, J. Phys.: Conf. Ser., 2265, 269–299, 2022.

Lanzilao, L. and Meyers, J.: An improved fringe-region technique for the representation of gravity waves in large eddy simulation with application to wind farms, Bound.-lay. Meteorol., 186, 567–593, 2023.

Lanzilao, L. and Meyers, J.: A parametric large-eddy simulation study of wind-farm blockage and gravity waves in conventionally neutral boundary layers, J. Fluid Mech., 979, 2024.

Maas, O. and Raasch, S.: Wake properties and power output of very large wind farms, Wind Energy Science, 7, 2022.

Mason, P. and Thomson, D.: Stochastic backscatter in large-eddy simulations of boundary layers, J. Fluid Mech., 242, 51–78, 1992.

Meyers, J.: Error-Landscape Assessment of Large-Eddy Simulations: A Review of the Methodology, Journal of Scientific Computing, 2011.

Meyers, J. and Meneveau, C.: Large eddy simulations of large wind-turbine arrays in the atmospheric boundary layer, 48th AIAA Aerospace Sciences Meeting, 2010.

Moeng, C.: A large-eddy-simulation model for the study of the planetary boundary-layer turbulence, Journal of Atmospheric Science, 41, 2052–2062, 1984.

Munters, W. and Meyers, J.: Dynamic strategies for yaw and induction control of wind farms based on large-eddy simulation and optimization, Energies, 11, 117, 2018.

Pedersen, J., Gryning, S.-E., and Kelly, M.: On the structure and adjustment of inversion-capped neutral atmospheric boundary-layer flows: large-eddy simulation study, Boundary-Layer Meteorology, 153, 2014.

Rampanelli, G. and Zardi, D.: A method to determine the capping inversion of the convective boundary layer, J. App. Meteorol., 43, 925–933, 2004.

Sanchez Gomez, M., Lundquist, J., Mirocha, J., and Arthur, R.: Investigating the physical mechanisms that modify wind plant blockage in stable boundary layers, Wind Energ. Sci.: Discussions, pp. 1–28, 2023.

Shapiro, C., Gayme, D., and Meneveau, C.: Filtered actuator disks: Theory and application to wind turbine models in large eddy simulation, Wind Energy, 22, 1414–1420, 2019.

Sood, I.: Development and validation of a large eddy simulation based virtual environment for optimal wind farm control. PhD thesis, KULeuven, Leuven, Belgium, 2023.

Steinbuch, M., de Boer, W., Bosgra, O., Peters, S., and Ploeg, J.: Optimal control of wind power plants, J. Wind Eng. Ind. Aerod., 27, 237–246, 1988.

Stevens, B., Moeng, C.-H., and Sullivan, P. P.: Entrainment and Subgrid Lengthscales in Large-Eddy Simulations of Atmospheric Boundary-Layer Flows, pp. 253–269, Springer Netherlands, Dordrecht, 2000.

Sullivan, P., Weil, J., Patton, E., Jonker, H., and Mironov, D.: Turbulent winds and temperature fronts in large-eddy simulations of the stable atmopsheric boundary-layer, Journal of the Atmospheric Sciences, 73, 2016.

Verstappen, R. and Veldman, A.: Symmetry-preserving discretization of turbulent flow, J. Comput. Phys., 187, 343–368, 2003.

Wu, Y. and Porté-Agel, F.: Large-eddy simulation of wind-turbine wakes: evalution of turbine parametrisations, Bound.-Lay. Meteorol., 138, 345–366, 2011.